Nanotechnology for Environmental Engineering (2021) 6:55
https://doi.org/10.1007/s41204-021-00151-y

ORIGINAL PAPER

Montmorillonite-anchored magnetite nanocomposite for recovery of ammonium from stormwater and its reuse in adsorption of Sc^{3+}

Jianzhi Song[1] · Varsha Srivastava[1] · Tomas Kohout[2] · Mika Sillanpää[3,4,5,6,7,8] · Tuomo Sainio[1]

Received: 7 June 2021 / Accepted: 28 August 2021 / Published online: 15 September 2021

Abstract

The treatment of stormwater to remove and recover nutrients has received increasing interest. The objective of this study was to develop a novel adsorbent that is easy to handle, has good adsorption capacity, and is economical to use. A novel nanocomposite of montmorillonite (MT)-anchored magnetite (Fe_3O_4) was synthesised by co-precipitation as an adsorbent for ammonium. The MT/Fe_3O_4 nanocomposite had pore sizes (3–13 nm) in the range of narrow mesopores. The dispersion of the anchored Fe_3O_4 was confirmed by transmission electron microscopy, scanning electron microscopy, and X-ray photoelectron spectroscopy (XPS). The nanocomposite exhibited higher affinity towards ammonium than the original MT. The Langmuir isotherm model was found to be the most suitable model to explain the ammonium adsorption behaviour of the nanocomposite. The maximum adsorption capacity for ammonium was 10.48 mg/g. The adsorption mechanism was a combination of ion exchange and electrostatic interaction. In an authentic stormwater sample, the synthesised adsorbent removed 64.2% of ammonium and reduced the amount of heavy metal contaminants including Mn, Ni, Cu and Zn. Furthermore, the ammonium loading on MT/Fe_3O_4 during adsorption functionalised the adsorbent surface. Additionally, the spent nanocomposite showed potential for rare earth elements (REEs) adsorption as a secondary application, especially for the selective adsorption of Sc^{3+}. The versatile application of montmorillonite-anchored magnetite nanocomposite makes it a promising adsorbent for water treatment.

Graphic abstract

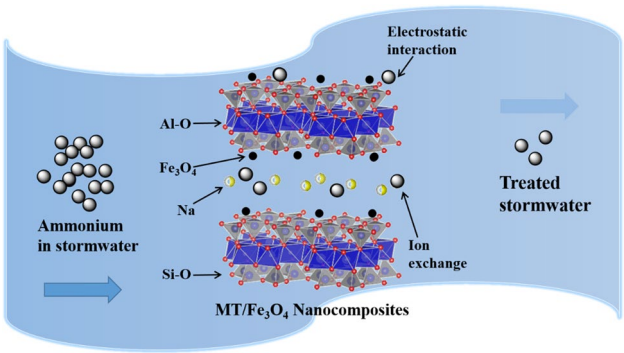

Keywords Stormwater · Montmorillonite · Magnetite · Nanocomposite · Ammonium recovery · REE recovery

Introduction

Urban living is replacing rural land use, increasing the size of impervious areas, reducing the availability of arable land, reducing infiltration and leading to increased surface runoff during storm events. Stormwater mobilises pollutant

✉ Tuomo Sainio
Tuomo.Sainio@lut.fi

Extended author information available on the last page of the article

loads (e.g. suspended solids, nutrients, metals, and oxygen-demanding matter) and transports them to receiving water bodies such as rivers, lakes and ponds [1–3]. Nutrients (ammonium and phosphate salts) accumulating in the aquatic environment result in eutrophication and algal blooms, causing the death of aquatic life and degradation of water quality [4]. Ammonium is conventionally removed by biologic processes through nitrification and denitrification. Then, it is finally converted to N_2 but with the presence of by-products such as nitrate [5–7]. Moreover, the ammonium content in stormwater varies throughout the year depending on the season and amount of precipitation; this has a negative impact on the biologic treatment. An abiotic process such as adsorption can recover ammonium with low energy consumption as well as deal with the fluctuations in ammonium concentration since adsorbents work efficiently with high concentrations of pollutants as well as trace amounts of contaminants [8–10]. Adsorption is also simple to execute and has low energy requirements [11]. For practical applications, adsorbents should be of low cost with high efficiency and easy recoverability.

Clay minerals are inexpensive, non-toxic natural materials which are widely used in the ceramic, paper, rubber, plastics, cosmetics and medicine industries. Among them is montmorillonite (MT), a one-dimensional crystal of aluminosilicate layers with interlayers of alkali metal and earth cations—typically Na^+, Ca^{2+}, and Mg^{2+}. It is a potential adsorbent owing to its large surface area, stable chemical properties and high cation exchange capacity [12, 13]. It was reported as an adsorbent with or without modification for the removal of copper (Cu^{2+}) [14] and ammonium [15]. The net negative charge on the structure of MT can attract and capture cations, making it a natural candidate for ammonium adsorption.

Recently, many efforts have been made for synthesis of adsorbent material by the incorporation of magnetic nanoparticles. As one of the popular inorganic nanoparticles [16] for wastewater treatment, magnetite (Fe_3O_4) possesses a high adsorption capacity and a fast adsorption rate. Furthermore, its magnetic feature allows for easy recovery after use [17, 18]. It was recently investigated as an adsorbent for the removal of cadmium (Cd^{2+}) [19]. Additionally, an ammonium-pillared MT/Fe_3O_4 nanocomposite was synthesised for caesium (Cs^+) removal from water and soil [20]. Moreover, the semiconductor properties of magnetite provide possible photocatalytic reactions—such as the degradation of organic pollutants—as an extra merit [21–24].

To the best of our knowledge, the use of the nanocomposite form of MT and Fe_3O_4 as adsorbents for ammonium recovery has not been reported. In this study, MT/Fe_3O_4 nanocomposites were synthesised using the co-precipitation method which consumes little power and is environmentally friendly [25] as a low-cost, non-toxic, easy-to-handle adsorbent for ammonium recovery in stormwater treatment. The characterisation of adsorbents—adsorption performance under various dosages, contact time, initial pH of ammonium solutions, initial concentration of ammonium solutions, kinetics, isotherm models, and stormwater treatment—has been studied thoroughly. Likewise, the ammonium-loaded nanocomposite was applied as an adsorbent for rare earth elements (REEs) recovery, especially for the selective adsorption of Sc^{3+}.

Materials and experimental methods

Materials

The montmorillonite (MT, K10 powder) was purchased from Sigma Aldrich. The chemicals used, including iron(II) chloride tetrahydrate ($FeCl_2{\cdot}4H_2O$), iron(III) chloride hexahydrate ($FeCl_3{\cdot}6H_2O$), ammonium chloride (NH_4Cl), sodium hydroxide (NaOH) and hydrochloric acid (HCl), were obtained from Sigma Aldrich and used without further purification.

Synthesis of MT/Fe_3O_4 nanocomposites

The method for the synthesis of Fe_3O_4 and MT/Fe_3O_4 nanocomposite was adapted from previous studies with minor modifications [20]. First, 1.8 g of $FeCl_2{\cdot}4H_2O$ was dissolved in 150 mL of deionised water. Then, MT was added to the solution in an ultrasonic bath for 10 min, and the mixture was stirred and heated in an oil bath for 20 min. Next, 2.7 g of $FeCl_3{\cdot}6H_2O$ was dissolved in the mixture and stirred for 30 min under N_2 flux at 80 °C, then 50 mL of NaOH (1.6 mol/L) solution was pumped into the mixture solution at a constant rate (0.5 or 2 mL/min) and stirred under N_2 atmosphere for times varying from 2 to 4 h. After the reaction, the suspension was centrifuged and washed thoroughly in ethanol and water. Finally, the solid product was dried in a hot air oven (Termaks) for 24 h at 60 °C.

Characterisation of adsorbent

MT/Fe_3O_4 nanocomposites synthesised in different conditions were thoroughly characterised using different techniques. The phase identification was done by X-ray Diffraction (XRD) in a PANalytical X-ray diffractometer using Co Kα irradiation at $\lambda = 1.79$ Å with 2θ ranging from 5° to 80° at 40 kV and 40 mA. The magnetic features of the synthesised adsorbents were characterised using a vibrating sample magnetometer (VSM, Princeton Measurements Micromag Model 3900); the field applied ranged from − 1.2 T to 1.2 T. Transmission electron microscopy (TEM) was conducted using a Hitachi HT-7700 at 100 kV. Its morphological and

elemental characteristics were evaluated through scanning electron microscopy (SEM) and energy-dispersive X-ray spectroscopy (EDS) in a Hitachi S-4800 microscope at 20 kV. Surface functional groups were identified by Fourier transform infrared spectroscopy (FTIR) using the Bruker Vertex 70 model in a spectra range of 4000–400 cm^{-1}. X-ray photoelectron spectroscopy (XPS) was done using a Thermo Fisher Scientific ESCALAB 250Xi (Thermo Fisher Scientific, UK), with an X-ray source of monochromatic Al Kα (1486.6 eV). The specific surface area and pore size distribution were determined by the N_2 Adsorption–desorption Isotherm (Tristar® II Plus). Samples were degassed at 60 °C under N_2 overnight and analysed using liquid nitrogen (77 K). The surface charge was investigated through a Surface Zeta Potential (ζ) study using a Malvern Zeta sizer Nano ZEN350 model; a 2 mg sample was dispersed in 10 mL of deionised water, and the pH was adjusted to 1–10 by HCl and NaOH.

Batch adsorption experiments for ammonium removal

The stock solution of ammonium was prepared by dissolving NH_4Cl in deionised water as 1,000 mg/L. The working solutions with desired concentrations were diluted from the stock solution. All the adsorption experiments were conducted using 15 mL tubes by mixing 10 mL of working solutions with known amounts of adsorbent. The tubes were shaken in an orbital shaker (IKA KS 4000 ic control) at a speed of 300 rpm for a given time at 25 °C or 35 °C. After shaking, the mixture was filtered using a 0.45 µm cellulose acetate syringe filter and analysed through Ion Chromatography (IC, Shimadzu; Shodex IC YS-50 column, column oven temperature 40 °C, 4 mM methanesulphonic acid eluent, pump flow 1 mL/min) for the concentrations of ammonium. The iron leaching from the adsorbents under different initial pH was analysed by inductively coupled plasma–optical emission spectrometry (ICP–OES, Thermo iCAP 6300 series) to determine the concentrations of iron in the treated solution after adsorption. The effects of adsorbent dosage, contact time, initial concentration and initial pH of working solutions were studied. The initial pH of working solutions was investigated in a range of 2 to 12 and adjusted by adding HCl (1 M and 0.1 M) and NaOH (1 M and 0.1 M). Adsorption experiments were also performed using real stormwater to investigate the efficiency of MT/Fe_3O_4 nanocomposites.

The amount of ammonium adsorbed was calculated from the mass balance, assuming constant liquid phase density:

$$q_e = \frac{V^L}{m_{ads}}\left(C_0 - C_e\right) \quad (1)$$

where q_e (mg/g) is the adsorbed amount, V^L (L) is the volume of liquid phase, m_{ads} (g) is the mass of adsorbent, and C_0 and C_e (mg/L) are the ammonium concentrations initially and at equilibrium, respectively. The removal efficiency RE was calculated by the following equation:

$$\mathrm{RE} = \frac{C_0 - C_e}{C_0} \times 100\% \quad (2)$$

Results and discussion

Preliminary adsorption experiments

Several batches of nanocomposite adsorbents were prepared by varying the amount of MT, the reaction time, and the flow rate of NaOH addition as listed in Table 1. The table also shows the preliminary characterisation of the surface area using the BET method.

Preliminary adsorption tests were conducted to determine the adsorbent batch with the highest uptake of NH_4^+. The initial NH_4^+ concentration was 50 mg/L, and the solid-to-liquid phase ratio was kept low (1:500 g/L) to avoid adsorbing all of ammonium which would yield only small differences in uptake between the adsorbent batches. Both the original MT and the prepared Fe_3O_4 showed limited removal efficiency of NH_4^+ at 4.90% and 2.52%, respectively, while the synthesised adsorbents were able to remove NH_4^+ with various efficiencies ranging from 16.58% to 37.20%.

The performance of the synthesised adsorbents with respect to NH_4^+ adsorption increased with retention time and the amount of MT used during synthesis. A possible reason for this is that the longer retention time ensures

Table 1 Adsorbent batches synthesised

MT/Fe_3O_4 ID	MT (g)	Time (h)	NaOH (mL/min)	S_{BET} (m^2/g)*	*RE* (%)**
Fe_3O_4	–	–	–	37.66	4.90
MT	–	–	–	245.99	2.52
517	1.0	2	0.5	92.86	16.58
522	2.0	2	0.5	129.65	17.61
529	3.0	2	0.5	122.70	25.29
528	3.0	4	0.5	128.68	28.70
603	4.0	4	0.5	88.22	30.34
604	4.0	4	2	100.17	37.20
605	5.0	4	0.5	98.16	32.33
610	5.0	4	2	123.32	24.73

* Specific surface area (BET)

**Solid-to-liquid phase ratio 1:500, initial NH_4^+ concentration 50 mg/L

better dispersion of Fe_3O_4 on the surface of the MT. The higher flow rates of NaOH pumped to the reaction lead to higher specific surface area (S_{BET}), but the NH_4^+ uptake ability changes depending on the amount of MT. The obvious improvement of the NH_4^+ uptake ability of MT after the modification indicates that the addition of iron creates and stimulates new active sites. However, excessive Fe_3O_4 may cover partial active sites resulting in lower removal efficiency of NH_4^+. As shown in Table 1, MT/$Fe_3O_4$604 has the highest adsorption towards NH_4^+. Therefore, further studies were conducted with sample MT/$Fe_3O_4$604 and reaction conditions were optimised for the enhancement of ammonium removal efficiency. The spent (ammonium loaded) adsorbent was then named MT/$Fe_3O_4$604N.

Characterisation of MT/Fe_3O_4 nanocomposites

Structure and magnetic properties

The crystal structures of MT, Fe_3O_4, and MT/Fe_3O_4 were investigated via XRD; the diffraction patterns (converted from Co Kα to Cu Kα) are shown in Fig. 1a. The seven strong peaks at 18.3°, 30.1°, 35.5°, 43.1°, 53.5°, 57.0°, and 62.7° corresponded to the cubic inverse spinel structure of Fe_3O_4, which was synthesised through co-precipitation of Fe^{2+} and Fe^{3+} [19, 26–28]. The diffraction peaks at 8.8°, 17.8°, 19.8°, 35.1°, and 45.5° corresponded to MT (montmorillonite K10), which were well matched with the reported spectra [29–31]. Quartz is present in MT, evidenced by the pattern at 20.8°, 26.6°, 50.1°, and 60.0° [32]. The spectra of MT/$Fe_3O_4$604 and MT/$Fe_3O_4$604N were almost the same as MT, suggesting that neither the modification by Fe_3O_4 nor the adsorption of NH_4^+ changed the crystal structure of MT. All the other MT/Fe_3O_4 nanocomposites expressed identical patterns, as shown in Fig. S1 in the Supplementary Document. The peak of Fe_3O_4 at 35.5°, presented beside the MT 35.1° (110) peak in the spectra of MT/$Fe_3O_4$604 and MT/$Fe_3O_4$604N, indicated that the (110) plane of MT/Fe_3O_4 became more disordered than that of MT due to the loading of Fe_3O_4.

The magnetic properties of the prepared MT/Fe_3O_4 products were evaluated by VSM, as shown in Figs. 1b and S2. All of the products exhibited superparamagnetic properties with extremely narrow hysteresis loops [33, 34]. Moreover, sample MT/$Fe_3O_4$517 (Fig. S2) had a relatively high saturation magnetisation, which is favourable for magnetic separation. The Fe_3O_4 aggregated to larger sizes due to the relatively high amount of it, resulting in low removal efficiency of MT/$Fe_3O_4$517. It was not selected as the sample to be further studied since the more important property is the high adsorption capacity. Although the magnetic moments of the products are relatively low, their magnetic feature can accelerate separation in the after-adsorption processes.

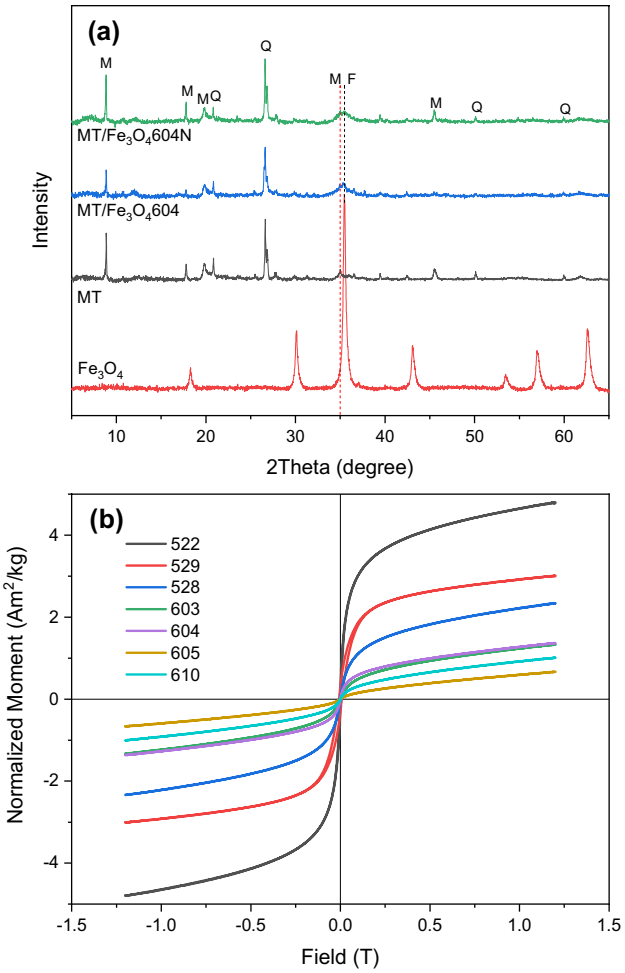

Fig. 1 **a** XRD patterns (M: montmorillonite, Q: quartz, F: Fe_3O_4), **b** hysteresis loops of the synthesised adsorbents. See Fig. S2 for data on sample 517

Morphology and composition analysis

The TEM images showed the sheet-like nature and small number of rod-like structures of MT (Fig. 2a) as well as the Fe_3O_4 nanoparticles and aggregates (Fig. 2b). The sizes of the Fe_3O_4 nanoparticles were around 15–25 nm, as shown in Fig. 2b. Similarly sized Fe_3O_4 nanoparticles were observed in the MT/Fe_3O_4 nanocomposites, as shown in Fig. 2c. The Fe_3O_4 nanoparticles were either dispersed on the surface and around the rod-like structures or intercalated between the layers of MT (Fig. 2c). This observation is confirmed by a SEM image of MT/$Fe_3O_4$604, as shown in Fig. 3c.

The morphologies of the representative samples were characterised by SEM, as shown in Fig. 3a-d. MT (Fig. 3a) had a shape of flakes and a layered, relatively smooth surface, while the Fe_3O_4 was in the shape of granules and seen on the surface of modified MT (Fig. 3c); this is direct evidence of the successful synthesis of MT/Fe_3O_4

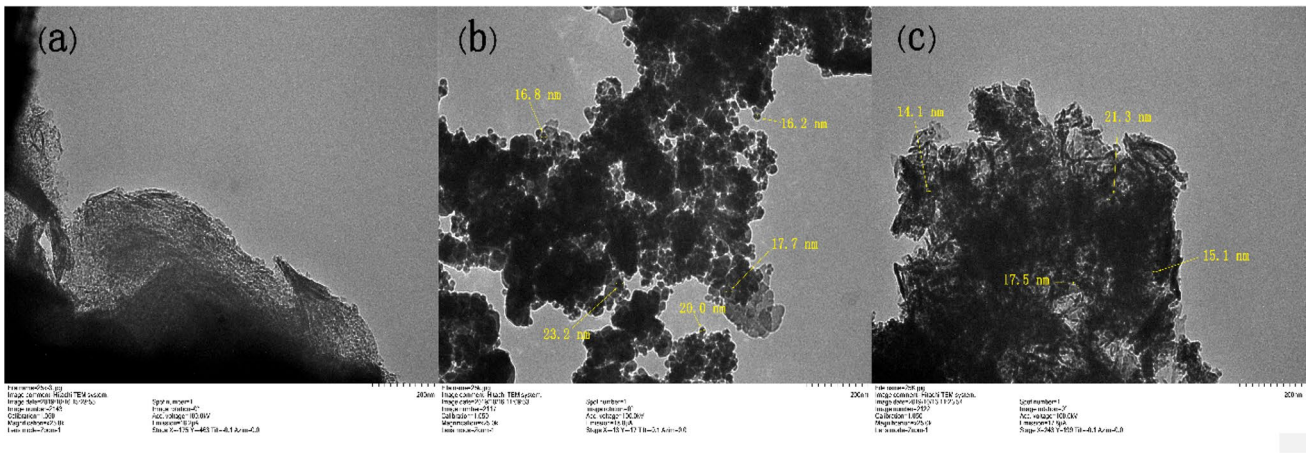

Fig. 2 TEM images of **a** MT, **b** Fe_3O_4, **c** MT/$Fe_3O_4$604

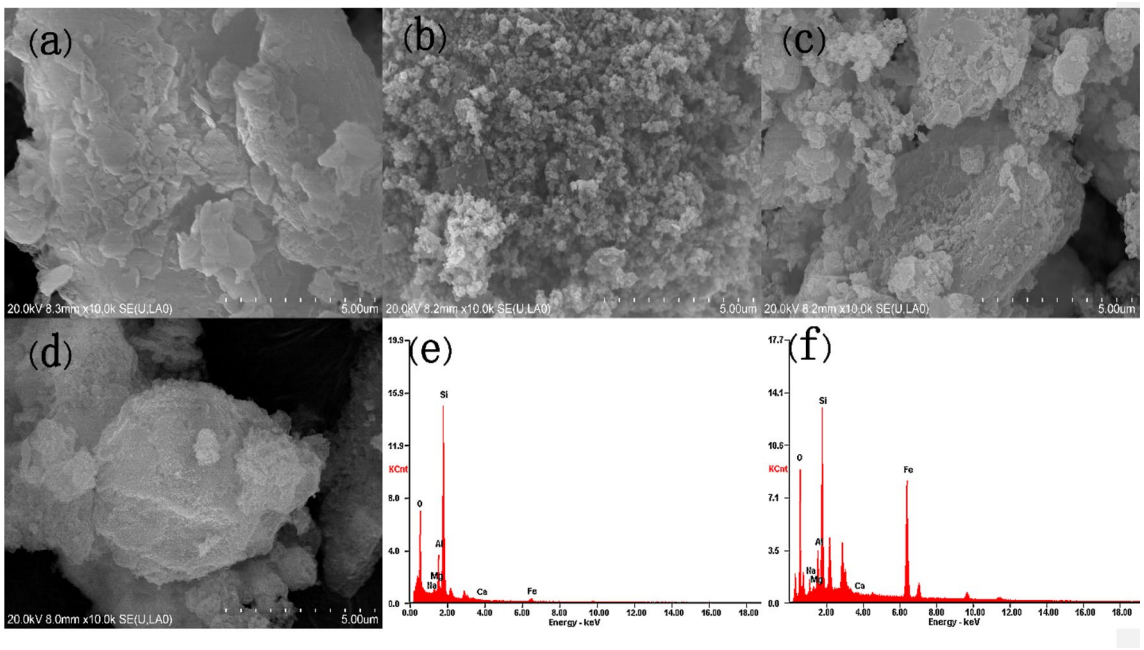

Fig. 3 SEM images of **a** MT, **b** Fe_3O_4, **c** MT/$Fe_3O_4$604, **d** MT/$Fe_3O_4$604N, EDS plots of **e** MT, **f** MT/$Fe_3O_4$604

nanocomposite [35]. The fine Fe_3O_4 particles adhere to the surface of MT as shown in Fig. 3c. The existence of Fe was confirmed by the EDS results (Fig. 3e-f), as the Fe content increased markedly in MT/$Fe_3O_4$604 compared to MT. After the adsorption process, the structure of MT/$Fe_3O_4$604N (Fig. 3d) was not significantly changed in compare with MT/$Fe_3O_4$604 (Fig. 3c), except for that the surface of MT/$Fe_3O_4$604N (Fig. 3d) was less covered by Fe_3O_4 particles which was corresponded by the iron leaching phenomenon (Fig. 6a).

The surface composition was analysed by XPS, as shown in Fig. 4a-b. Peaks at 724.9 eV and 711.4 eV—as two typical spectra of Fe $2p_{1/2}$ and Fe $2p_{3/2}$, respectively—confirmed the existence of Fe_3O_4 in the as-synthesised adsorbents [36, 37]. The Mg 1s peak was present in the spectrum of MT, but barely showed after modification, indicating that Fe took the place of Mg. As expected, N 1s appeared in the spectrum of MT/$Fe_3O_4$604N after adsorption, as evidence of the existence of NH_4^+ on the surface of the MT/Fe_3O_4 nanocomposite. The characteristic peak of Si 2p verified the composition of MT [20]. The binding energy of Si 2p increased by 1.2 eV from MT to MT/$Fe_3O_4$604, indicating a strong interaction between Si and Fe atoms. The lowered intensity of Si 2p in MT/Fe_3O_4 nanocomposite compared with MT suggests that partial Si sites were covered by Fe_3O_4. The Na 1s was not observed in MT but appeared clearly in the MT/Fe_3O_4

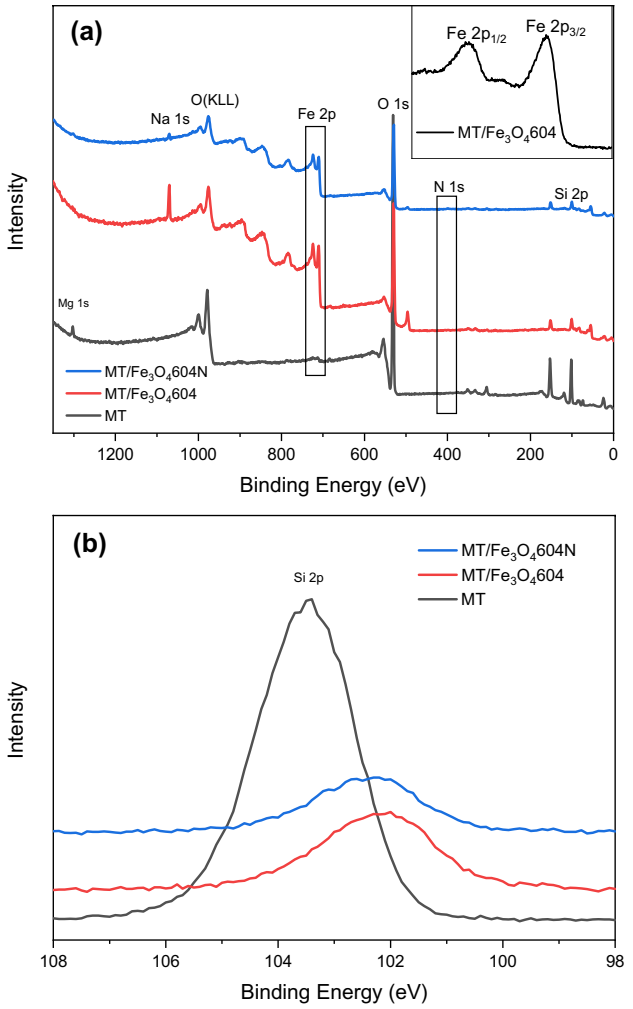

Fig. 4 XPS spectra of adsorbent materials **a** survey, **b** Si 2p

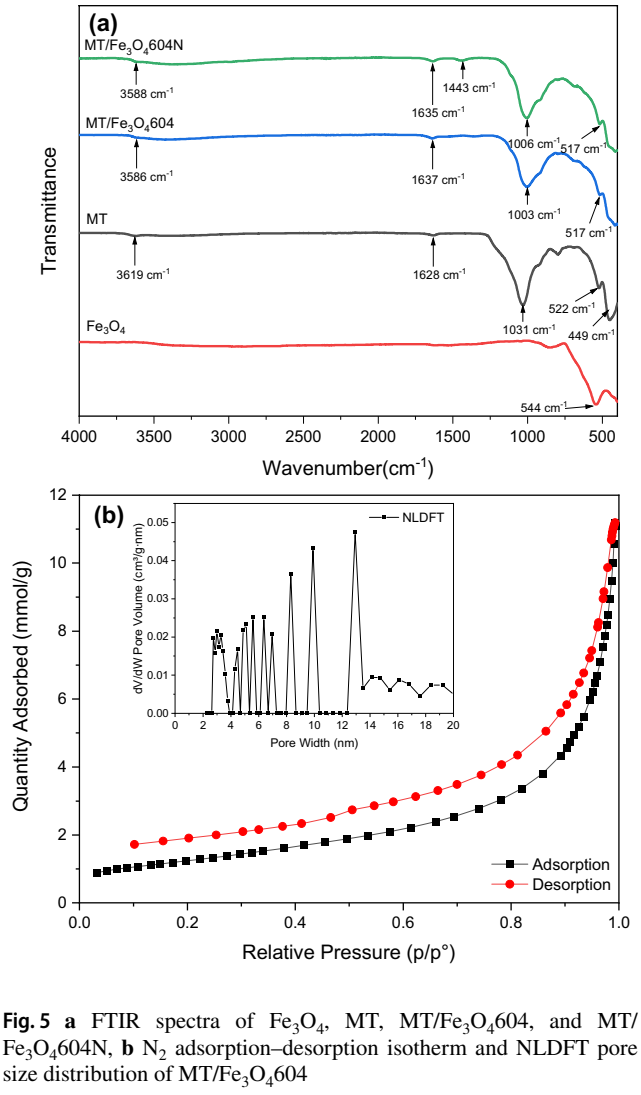

Fig. 5 **a** FTIR spectra of Fe_3O_4, MT, MT/$Fe_3O_4$604, and MT/$Fe_3O_4$604N, **b** N_2 adsorption–desorption isotherm and NLDFT pore size distribution of MT/$Fe_3O_4$604

nanocomposite (Fig. S3), coming from the NaOH used in the modification. During the adsorption process, Na was released to the aqueous solution, so there was a low-intensity peak of Na 1s in the used adsorbent (MT/$Fe_3O_4$604N).

The infrared spectra of MT, Fe_3O_4 and the adsorbent before and after the adsorption of NH_4^+ are shown in Fig. 5a. The band at 544 cm^{-1} in the spectra of Fe_3O_4 corresponds to the characteristic band of magnetite, which is attributed to the mixture of Fe^{2+} and Fe^{3+} in the sample [38, 39]. The characteristic strong bands at 1,031 and 449 cm^{-1} of MT are assigned to the stretching of Si–O. The Si–O bands are present in the spectra of modified samples at around 1000 cm^{-1}. The bands showed at around 3600 and 1630 cm^{-1} are related to the stretching and bending of hydroxyl groups, respectively [40, 41]. The shifting of Si–O and hydroxyl groups from MT to MT/$Fe_3O_4$604 indicated that the loaded Fe_3O_4 encountered these groups on the surface of MT. One new band appeared in the spectra of the after-adsorption sample at 1,443 cm^{-1} due to the deformation of NH_4^+, indicating that chemisorption of NH_4^+ happened during the contact [15]. The bands at around 520 cm^{-1} are attributed to the vibrations of the Si–O–Al structure [20].

Specific surface area and pore size analysis

According to IUPAC classification, the N_2 adsorption–desorption isotherm of MT/$Fe_3O_4$604 (Fig. 5b) is a Type IV physisorption isotherm and Type H3 hysteresis loop, given by non-rigid aggregates of plate-like particles; in this case, it is montmorillonite, with slit-shaped pores. The Kelvin equation-based Barrett–Joyner–Halenda (BJH) method would underestimate the pore size for narrow mesopores, so the non-local-density functional theory (NLDFT)-based method was applied to obtain a more reliable assessment of pore size distribution [42]. As shown in Fig. 5b, the pore sizes of MT/$Fe_3O_4$604 are distributed in the range of narrow mesopores, which are in the range of 3–13 nm. The particle size of MT/Fe3O4604 was analysed by Zeta sizer, found to

be 609.4 nm in diameter. The physical dimensions of the pores suggest a good molecular sieving effect, which indicate that the nanocomposite can be used as a filling material to be dispersed into polymer matrices of membranes for a better separation performance in water treatment [43, 44].

The S_{BET} was calculated by the Brunauer–Emmett–Teller (BET) method and listed in Table 1. The raw MT has the highest S_{BET} of 245.99 m^2/g, while all the MT/Fe_3O_4 nanocomposites have lower S_{BET}. There is no clear trend of surface area among the prepared adsorbent samples based on the MT amount for the reaction, but the flow rate of NaOH affected the S_{BET} in a such a way that the higher flow rate (2 mL/min) led to a higher S_{BET} than that of the lower flow rate (0.5 mL/min) when the MT amount and retention time were the same.

This is possibly due to the behaviour of Fe_3O_4 aggregates on the MT surface; more Fe_3O_4 was formed inside the pores of MT at a lower rate. The results also suggested that the adsorptive property need not always be positively correlated to the specific surface area. It is noteworthy that the best adsorption capacity was obtained with MT/$Fe_3O_4$604 even though the highest S_{BET} was attained with MT/$Fe_3O_4$522. The main difference is higher MT/Fe ratio and longer reaction time in the synthesis of MT/$Fe_3O_4$604.

Adsorption mechanism and kinetics

Adsorption mechanism

A series of adsorption equilibrium studies were performed with initial NH_4^+ concentrations of 10 to 80 mg/L at 25 and 35 °C. These are typical ambient temperatures in many geographic regions. Higher temperatures were not studied because the high energy requirement for stormwater heating was not economic. The concentrations of NH_4^+ in stormwater vary throughout seasons. Therefore, concentrations ranging up to 80 mg/L were appropriate.

NH_4^+ uptake increased with increasing initial concentration of NH_4^+ (Fig. 6b), meaning that some of the available active sites remain unoccupied at lower NH_4^+ concentrations. Similar results were observed in other studies on the adsorption of NH_4^+ by clay and Fe_3O_4 materials [45, 46]. Additionally, higher equilibrium loading was achieved at 35 °C than at 25 °C, which suggests that the adsorption process is endothermic.

The pH of the NH_4^+ solution influences the adsorption process. Therefore, the adsorption of ammonium ions by MT/$Fe_3O_4$604 was also investigated in different pH ranges. 50 mg/L NH_4^+ solution was adjusted to an initial pH of 2, 4, 6, 7, 8, 10, and 12, respectively, and contacted with MT/$Fe_3O_4$604 through shaking at 300 rpm for 60 min at 25 °C. As shown in Fig. 6a, the abundant H^+ ions inhibited the adsorption of NH_4^+ in highly acidic conditions (pH 2) through competitive adsorption [47] while the adsorption amounts of NH_4^+ under other pH conditions are affected to some extent. This may have been because the added adsorbents affected the pH of the solutions, resulting in a reduction in the effect of the initial pH of the NH_4^+ solutions on the adsorption behaviour.

A possible issue with the nanocomposite adsorbent is dissolution of iron. A high solid-to-liquid phase ratio of 1:4 was used to observe this phenomenon even if leaching was low. As observed in Fig. 6a, iron leaching was significant at pH 2 (51.3 mg/L) but negligible at pH ranging from 4 to 10 (< 0.85 mg/L). Leaching of iron increased again under alkaline conditions (pH 12, 1.43 mg/L). Therefore, we conclude that the nanocomposite adsorbents are stable at the pH range of their most likely applications.

The cations in the MT framework contributed to the removal of NH_4^+ by MT/Fe_3O_4 nanocomposite through ion

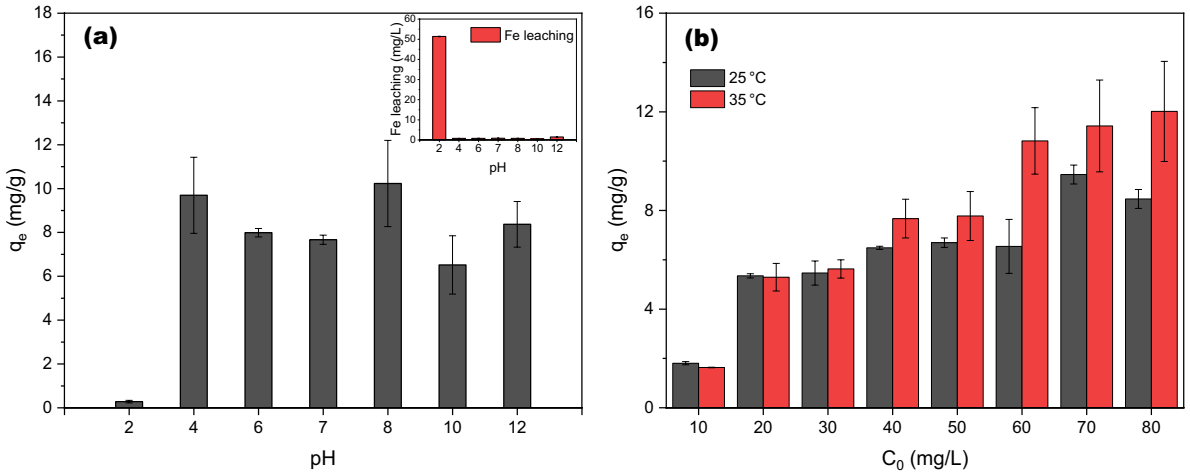

Fig. 6 Influence of pH and temperature on adsorption of ammonium at initial concentrations of 10 to 80 mg/L at 25 °C and 35 °C

exchange [48, 49]. It was indicated in the results of XPS and stormwater test that Na^+ took the role of ion exchange during the contact of MT/$Fe_3O_4$604 and the NH_4^+-containing solution. Meanwhile, co-existing cations such as K^+, Mg^{2+}, and Ca^{2+} worked as competitive cations during the removal of NH_4^+.

As shown in Fig. 7a, we further investigated the zeta potential (ζ) of MT, Fe_3O_4, and MT/$Fe_3O_4$604, dispersing it in deionised water at different pH values. The surface charge features of MT were in accordance with the literature [15]. The loading of Fe_3O_4 particles changed the zeta potential variation of MT. The isoelectric point (pH point of zero charge, pH_{pzc}) of MT/$Fe_3O_4$604 was 5.01, close to that of Fe_3O_4, which was 4.80. The similarity of MT/$Fe_3O_4$604 and Fe_3O_4 revealed the successful coating of Fe_3O_4 on the surface of MT [50]. At $pH > pH_{pzc}$, MT/$Fe_3O_4$604 was negatively charged, which is favourable for electrostatic interaction with cationic NH_4^+ [51].

Based on the analysis above, the mechanism (Scheme 1) of the uptake of NH_4^+ by the MT/Fe_3O_4 nanocomposite may be pictured as the following reactions, which contribute to ion exchange and electrostatic interaction, respectively. The sodium ions (Na^+) existing in the interlayers of MT/Fe_3O_4 nanocomposite exchange with NH_4^+ during the adsorption procedure, as shown in Eq. (3). The MT/Fe_3O_4 nanocomposite exhibits a negative charge at a pH that is higher than 5. Thus, NH_4^+ can be captured through electrostatic interaction, Eq. (4).

$$\mathrm{Na-MT/Fe_3O_4 + NH_4Cl \rightleftharpoons NH_4-MT/Fe_3O_4 + NaCl} \tag{3}$$

$$\mathrm{MT/Fe_3O_4^- + NH_4^+ \rightleftharpoons NH_4^+ \bullet MT/Fe_3O_4^-} \tag{4}$$

Adsorption isotherms

The adsorption isotherms were studied by correlating them with Langmuir, Freundlich, and Fowler–Guggenheim isotherm models [52–55]. The Langmuir isotherm [56] is written as

$$q_e = \frac{q_m K_L C_e}{1 + K_L C_e} \tag{5}$$

where C_e (mg/L) is the concentration of NH_4^+ in equilibrium, q_e (mg/g) and q_m (mg/g) are the amount of NH_4^+ adsorbed in equilibrium and the maximum uptake, respectively, and K_L (L/mg) is the Langmuir constant.

The equation for Freundlich isotherm [57] is

$$q_e = K_f C_e^{\frac{1}{n}} \tag{6}$$

where n represents the heterogeneity factor related to the distribution of interaction energies of adsorption sites, and K_f (mg/g·(L/mg)$^{1/n}$) is the Freundlich constant.

The Fowler–Guggenheim isotherm (Eq. 7) assumes an energetically homogeneous adsorbent surface like the Langmuir isotherm but includes an additional parameter to describe interactions between adsorbed species. Such interactions can be positive or negative (*i.e.* lead to increased or decreased surface concentration on the adsorbent). While the model is not explicit, solving Eq. (7) for the equilibrium loading q_e is straightforward with standard numerical methods.

$$K_{FG} C_e = \frac{q_e}{q_m - q_e} \exp\left(-\chi \frac{q_e}{q_m}\right) \tag{7}$$

In Eq. (7), K_{FG} and q_m have the same meaning as the corresponding parameters in the Langmuir isotherm. χ describes the lateral interactions between adsorbed molecules.

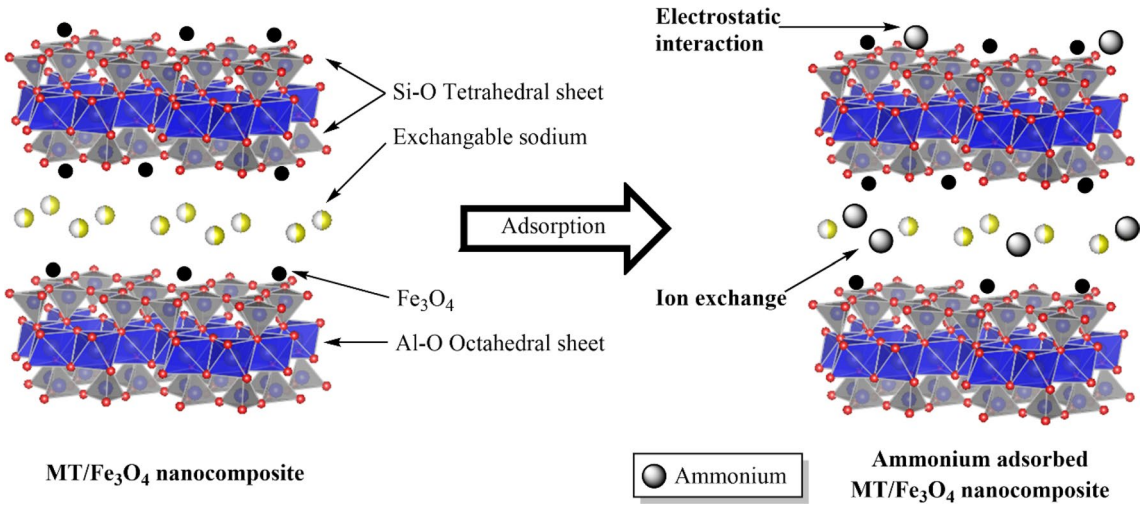

Scheme 1 Mechanism of ammonium adsorption on MT/Fe_3O_4 nanocomposite

To avoid artefacts arising from linearising the isotherm models and data, the parameters of the isotherm models were fitted with the nonlinear least squares method. The best-fit values are listed in Table 2, and plots for adsorption at 25 °C are shown in Fig. 7b. The Langmuir isotherm model was best model to explain the NH_4^+ adsorption at 25 °C, indicating monolayer adsorption to a finite number of adsorption sites. The Freundlich model predicts unreasonably high ammonia uptake at low concentrations. The Fowler–Guggenheim model, which includes interaction between adsorbed molecules, gives a somewhat higher R^2 than the Langmuir isotherm. However, it fails to predict the increase of loading beyond 8 mg/g in the high concentration range. The lateral interaction parameter, $\chi = 2.43$, is quite large, suggesting a strong attractive interaction between adsorbed species. Considering that ammonium is charged, it is unlikely that this is the case. We therefore concluded that the improved fit is only due to the additional degree of freedom and that the model is overparameterised.

The maximum Langmuir adsorption capacity was found to be 10.48 mg/g for MT/$Fe_3O_4$604 towards NH_4^+. This capacity is comparable to or better than reported for other clay-based materials (Table 3). For example, a capacity of 12.5 mg/g for NH_4^+ on montmorillonite-biochar composites has been reported [58]. On the other hand, capacities of 1.54 mg/g and 1.38 mg/g have been reported for montmorillonite nano-clay and natural vermiculite, respectively [59]. Significantly higher capacity (40.4 mg/g) has been reported for NH_4^+ uptake in montmorillonite, but the liquid phase concentration was tenfold that in this study [15]. At conditions comparable to this study, however, the uptake in montmorillonite was slightly lower than here ($q_e = 7$ mg/g at $C_e = 60$ mg/L) [15].

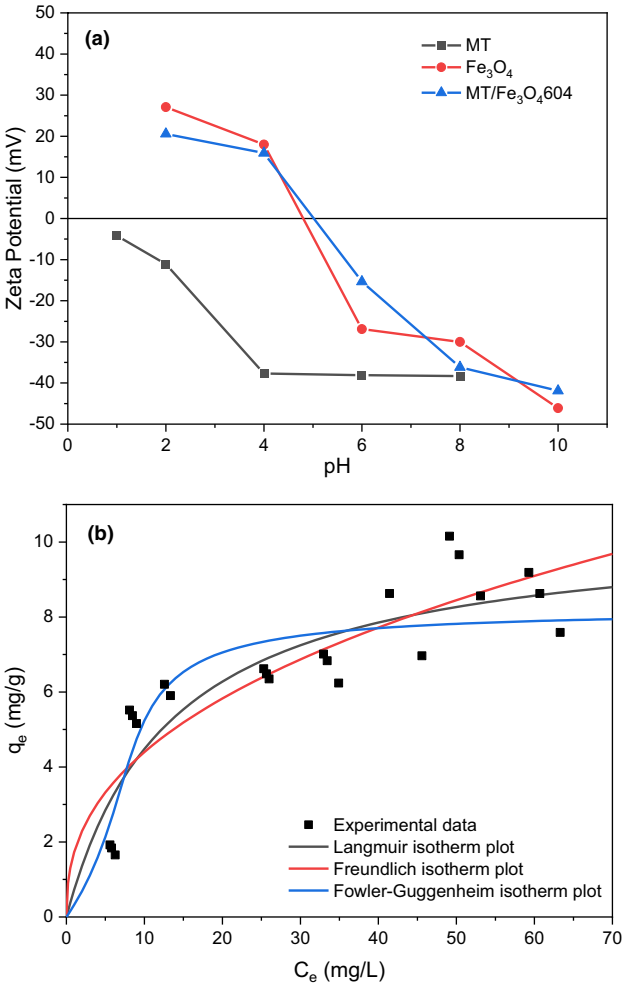

Fig. 7 **a** Zeta potential plots, **b** isotherm models

Adsorption kinetics

The adsorption kinetics were studied in a batch adsorber using 2.5 g/L adsorbent dosage and initial NH_4^+ concentrations of 30 mg/L, 50 mg/L, and 80 mg/L. As shown in Fig. 8, the NH_4^+ uptake reaches a high level within 5 min for 30 mg/L, and within 3 min for 50 and 80 mg/L. The batch method is not well suited for such fast adsorption; the data are not accurate enough for discrimination between kinetic models. Nevertheless, the intra-particle diffusion model that assumes Fickian diffusion in a homogeneous medium with constant boundary conditions was applied to check if

Table 2 Parameters of the isotherm models and goodness of fit to equilibrium data

Isotherm	Parameters			R^2
Langmuir	q_m (mg/g)	K_L (L/mg)		0.8841
	10.48	0.075		
Freundlich	n	K_f (mg/g·(L/mg)$^{1/n}$)		0.8731
	2.46	1.73		
Fowler–Guggenheim	q_m (mg/g)	K_{FG} (L/g)	χ	0.8935
	8.24	0.037	2.43	

Table 3 Comparison of adsorption capacities of similar adsorbents for NH_4^+

Adsorbent	Adsorption capacity (mg/g)	References
MT/Fe_3O_4 nanocomposite	10.48	Current study
MT nano-clay	1.54	[59]
Natural vermiculite	1.38	[59]
MT biochar composite	12.52	[58]
Natural MT	40.4	[15]

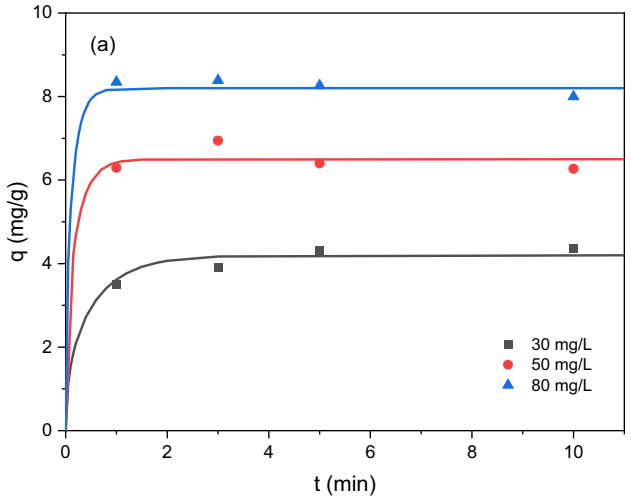

Fig. 8 Ammonium adsorption kinetics. Lines are calculated with Fickian intra-particle diffusion model (Eq. 8)

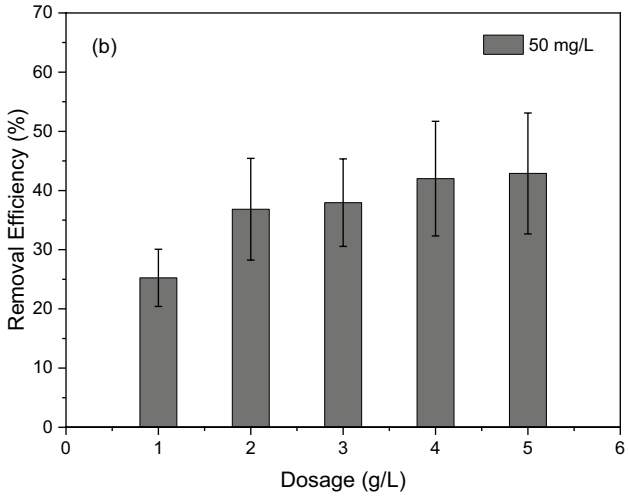

Fig. 9 Effect of adsorbent dosage on ammonium removal efficiency

intra-particle diffusion resistance could explain the results. The loading as a function of time was calculated from Eq. (8)

$$q = q_{\mathrm{eq}}\left(1 - \frac{6}{\pi^2}\sum_{j=1}^{\infty}\frac{1}{j^2}\exp\left(-j^2\pi^2 D' t\right)\right) \tag{8}$$

where q and q_{eq} (mg/g) are the amount adsorbed at time t and at equilibrium, and D' (1/s) is the mass transfer parameter that includes the diffusion coefficient and the (unknown) Sauter mean diameter of the particles. The infinite series was truncated at $j = 30$, which is more than sufficient as the series converges rapidly (*e.g.* below 1e-17 with $j = 15$ at $t = 0.1$ min). As observed in Fig. 8, this model fits reasonably well to the data, suggesting that the intra-particle diffusion is the sole rate-limiting step [60, 61]. The mass transfer parameter D' was found to increase with increasing initial concentration (and thus loading). Values of 0.15 1/s, 0.40 1/s and 0.60 1/s were obtained with initial concentrations 30 mg/L, 50 mg/L and 80 mg/L, respectively. Since ammonium adsorption is strongly nonlinear, this suggests that diffusion may take place also in the adsorbed phase.

Ammonium removal from authentic stormwater

Application of the adsorbent to remove ammonium from an authentic stormwater was studied at laboratory scale. The operating conditions and suitable adsorbent dosing were first determined in preliminary tests.

The adsorbent dosage was varied from 1 to 5 g/L, studied using 50 mg/L NH_4^+ solution, shaking at 300 rpm for 120 min at 25 °C. The removal efficiency of NH_4^+ increased with increasing dosage due to the increased active sites for NH_4^+ adsorption which increased the uptake amount. As shown in Fig. 9, the removal efficiency was improved by more than 10 percentage points from 1 to 3 g/L, but less than 5 percentage points from 3 to 5 g/L. This is typical for Langmuir-type adsorption and originates from the decrease in the equilibrium concentration when the adsorbent dosage increases. Considering the cost and removal efficiency, 2.5 g/L was selected as the optimal dosage for a single-contact adsorption process; this was used in the subsequent adsorption studies.

The adsorption efficiency of MT/$Fe_3O_4$604 was investigated for real stormwater collected from the landfill factory Metsäsairila Oy in Mikkeli, Finland, on August 19, 2019. The sample was filtered and used as a working solution directly for adsorption at conditions of 2.5 g/L dosage, shaking at 300 rpm for 1 h at 25 °C. The contents of the stormwater were examined by ICP-OES for Na, Mg, Al, K, Ca, Cr, Mn, Fe, Co, Ni, Cu, and Zn; all these elements were detected except Cr and Co, which were under the detection limit.

NH_4^+ removal efficiency reached 64.2% as shown in Fig. 10. Simultaneously, the concentrations of Mg, K, and Ca in the stormwater were reduced significantly. Heavy metals, including Mn, Ni, Cu, and Zn, were diminished to zero or nearly zero. Na as well as a small amount of Al were released by the adsorbent, which confirms the role of ion exchange mechanism. As previously discussed, Fe leaching was low since the pH of stormwater was 6.54. Overall, the new adsorbent recovered NH_4^+ well in the presence of other metallic ions during treatment of stormwater. The additional benefit of eliminating heavy metals such as Mn, Ni, Cu, and Zn to extremely low concentrations (in current case ≤ 0.1 mg/L, which is lower than the detection limit of ICP-OES) is notable.

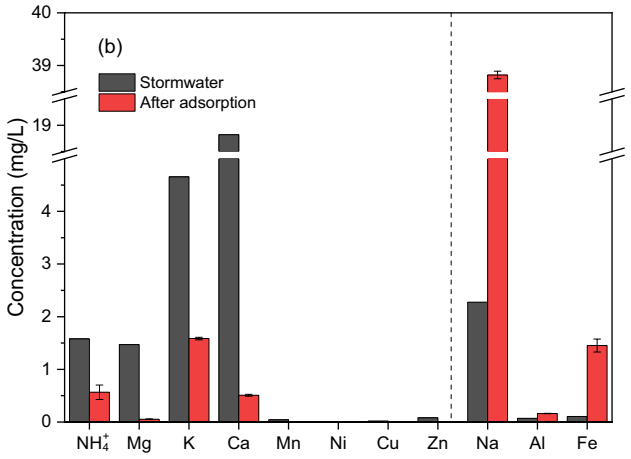

Fig. 10 Removal of ammonium and other cations from authentic stormwater using adsorbent MT/$Fe_3O_4$604 (solid-to-liquid phase ratio 1:400)

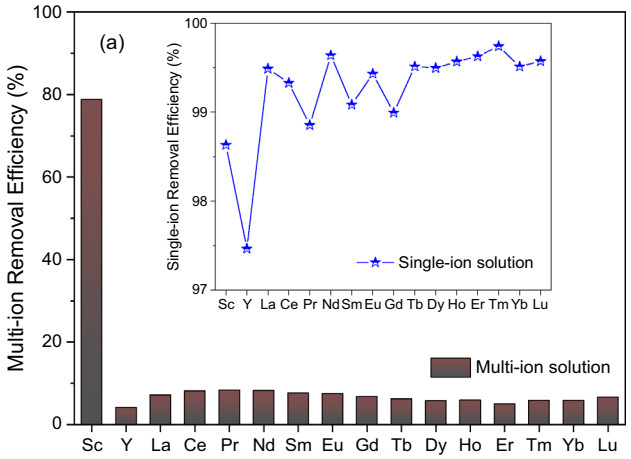

Fig. 11 Removal efficiency of spent (ammonium loaded) MT/$Fe_3O_4$604 for recovery of REEs from aqueous solution

Potential of reusing NH_4^+ loaded adsorbents in REE recovery

To improve the economics of adsorptive ammonium removal from stormwater, we studied the reuse of the spent (ammonium loaded) adsorbent in a secondary application. Utilising the ammonium ion-loaded adsorbents for selective recovery of valuable elements avoids the generation of chemical waste from the regeneration of adsorbents. To this end, the adsorbents were first loaded with 50 mg/L NH_4^+ solution; then, the uptake of REEs from aqueous solution was studied. The REEs used for the study include scandium (Sc), yttrium (*Y*), and all the lanthanides except promethium (Pm). The adsorption study was conducted at conditions of 2.5 g/L dosage, 20 mg/L working solution, shaking at 300 rpm for 1 h at 25 °C.

As observed in Fig. 11, the used MT/Fe_3O_4 nanocomposite achieved almost 100% removal efficiency for all 16 REE ions in the single-REE containing solutions. In the mixture of all REEs, the adsorbent showed selective affinity towards Sc^{3+}. The results indicate that the spent (ammonium loaded) MT/Fe_3O_4 nanocomposite possesses the potential for REE recovery as a secondary application, especially for selective adsorption of Sc^{3+} among other REEs. However, regeneration of the adsorbent to recover REEs was not studied.

Conclusions

In this study, the nanocomposite of montmorillonite-anchored magnetite was synthesised and studied for the removal of ammonium in stormwater. FTIR, XRD and XPS confirmed the successful loading of Fe_3O_4 onto MT. The Fe_3O_4 enhanced the adsorption of NH_4^+ and provided magnetic features to MT, which accelerated the separation of the adsorbent from water. It was observed that the adsorption was influenced by dosage, contact time, initial concentration, and pH. The adsorption behaviour of NH_4^+ was well expressed by pseudo-second-order kinetics and the Temkin isotherm model. Both ion exchange and electrostatic interaction contributed to its affinity for NH_4^+. The adsorbent MT/$Fe_3O_4$604 was able to treat real stormwater, reducing the NH_4^+ as well as heavy metal contents. Moreover, the ammonium-loaded nanocomposite possesses the potential for REE recovery as a secondary application, especially for the selective adsorption of Sc^{3+} among other REEs. Further study regarding the desorption of Sc^{3+} could be conducted to affirm and maximize the recovery potential. This study suggests that MT/Fe_3O_4 nanocomposites are potential adsorbents for stormwater treatment regarding NH_4^+ recovery. Furthermore, the nanocomposites could be utilised as functional material in a membrane or in polymer beads that are better suitable for large scale water treatment operations than powders [62, 63].

Appendix A. Supplementary data

Supplementary data associated with this article can be found in the online version.

Supplementary Information The online version contains supplementary material available at https://doi.org/10.1007/s41204-021-00151-y.

Acknowledgements This work was supported by the European Regional Development Fund (ERDF, project ID A73961) and the Academy of Finland (decision number 315051).

Funding Open access funding provided by LUT University (previously Lappeenranta University of Technology (LUT)).

Declarations

Conflict of interest On behalf of all authors, the corresponding author states that there is no conflict of interest.

References

1. Goonetilleke A, Lampard J-L (2019) Stormwater quality, pollutant sources, processes, and treatment options. In: Approaches to water sensitive urban des. Woodhead Publishing, pp 49–74. https://doi.org/10.1016/B978-0-12-812843-5.00003-4
2. Yue C, Li LY, Johnston C (2018) Exploratory study on modification of sludge-based activated carbon for nutrient removal from stormwater runoff. J Environ Manage 226:37–45. https://doi.org/10.1016/J.JENVMAN.2018.07.089
3. Tian J, Miller V, Chiu PC, Maresca JA, Guo M, Imhoff PT (2016) Nutrient release and ammonium sorption by poultry litter and wood biochars in stormwater treatment. Sci Total Environ 553:596–606. https://doi.org/10.1016/J.SCITOTENV.2016.02.129
4. Jones J, Chang N-B, Wanielista MP (2015) Reliability analysis of nutrient removal from stormwater runoff with green sorption media under varying influent conditions. Sci Total Environ 502:434–447. https://doi.org/10.1016/J.SCITOTENV.2014.09.016
5. Mohanty SK, Valenca R, Berger AW, Yu IKM, Xiong X, Saunders TM, Tsang DCW (2018) Plenty of room for carbon on the ground: Potential applications of biochar for stormwater treatment. Sci Total Environ 625:1644–1658. https://doi.org/10.1016/J.SCITOTENV.2018.01.037
6. Ye Y, Ngo HH, Guo W, Liu Y, Chang SW, Nguyen DD, Liang H, Wang J (2018) A critical review on ammonium recovery from wastewater for sustainable wastewater management. Bioresour Technol 268:749–758. https://doi.org/10.1016/J.BIORTECH.2018.07.111
7. Yan T, Ye Y, Ma H, Zhang Y, Guo W, Du B, Wei Q, Wei D, Ngo HH (2018) A critical review on membrane hybrid system for nutrient recovery from wastewater. Chem Eng J 348:143–156. https://doi.org/10.1016/J.CEJ.2018.04.166
8. Srivastava V, Iftekhar S, Wang Z, Babu I, Sillanpää M (2018) Synthesis and application of biocompatible nontoxic nanoparticles for reclamation of Ce3+ from synthetic wastewater: toxicity assessment, kinetic, isotherm and thermodynamic study. J Rare Earths 36:994–1006. https://doi.org/10.1016/J.JRE.2018.03.005
9. Ramasamy DL, Khan S, Repo E, Sillanpää M (2017) Synthesis of mesoporous and microporous amine and non-amine functionalized silica gels for the application of rare earth elements (REE) recovery from the waste water-understanding the role of pH, temperature, calcination and mechanism in Light REE and Heavy REE separation. Chem Eng J 322:56–65. https://doi.org/10.1016/J.CEJ.2017.03.152
10. Ramasamy DL, Repo E, Srivastava V, Sillanpää M (2017) Chemically immobilized and physically adsorbed PAN/acetylacetone modified mesoporous silica for the recovery of rare earth elements from the waste water-comparative and optimization study. Water Res 114:264–276. https://doi.org/10.1016/J.WATRES.2017.02.045
11. Srivastava V, Sillanpää M (2017) Synthesis of malachite@clay nanocomposite for rapid scavenging of cationic and anionic dyes from synthetic wastewater. J Environ Sci 51:97–110. https://doi.org/10.1016/J.JES.2016.08.011
12. Jacobs JD, Koerner H, Heinz H, Farmer BL, Mirau P, Garrett PH, Vaia RA (2006) Dynamics of alkyl ammonium intercalants within organically modified montmorillonite: dielectric relaxation and ionic conductivity. J Phys Chem B 110:20143–20157. https://doi.org/10.1021/jp0619311
13. Peng C, Zhong Y, Min F (2018) Adsorption of alkylamine cations on montmorillonite (001) surface: a density functional theory study. Appl Clay Sci 152:249–258. https://doi.org/10.1016/J.CLAY.2017.11.021
14. Bhattacharyya KG, Sen Gupta S (2006) Kaolinite, montmorillonite, and their modified derivatives as adsorbents for removal of Cu(II) from aqueous solution. Sep Purif Technol 50:388–397. https://doi.org/10.1016/J.SEPPUR.2005.12.014
15. Alshameri A, Zhu R, Ma L, Tao Q (2018) Adsorption of ammonium by different natural clay minerals: characterization, kinetics and adsorption isotherms. Appl Clay Sci 159:83–93. https://doi.org/10.1016/J.CLAY.2017.11.007
16. Nabi G, Qurat-ul-Aain NR, Khalid MB, Tahir M, Rafique M, Rizwan S, Hussain T, Iqbal AM (2018) A Review on novel ecofriendly green approach to synthesis tio2 nanoparticles using different extracts. J Inorg Organomet Polym Mater 28:1552–1564. https://doi.org/10.1007/s10904-018-0812-0
17. Nassar NN (2012) Iron oxide nanoadsorbents for removal of various pollutants from wastewater: an overview. In: Application of adsorbents for water pollution control. Bentham Science Publishers, Sharjah, pp 81–118
18. Liu F, Zhou K, Chen Q, Wang A, Chen W (2018) Preparation of magnetic ferrite by optimizing the synthetic pH and its application for the removal of Cd(II) from Cd-NH3-H2O system. J Mol Liq 264:215–222. https://doi.org/10.1016/J.MOLLIQ.2018.05.038
19. Liu F, Zhou K, Chen Q, Wang A, Chen W (2019) Application of magnetic ferrite nanoparticles for removal of Cu(II) from copper-ammonia wastewater. J Alloys Compd 773:140–149. https://doi.org/10.1016/j.jallcom.2018.09.240
20. Zheng X, Dou J, Yuan J, Qin W, Hong X, Ding A (2017) Removal of Cs+ from water and soil by ammonium-pillared montmorillonite/Fe3O4 composite. J Environ Sci 56:12–24. https://doi.org/10.1016/j.jes.2016.08.019
21. Fadillah G, Yudha SP, Sagadevan S, Fatimah I, Muraza O (2020) Magnetic iron oxide/clay nanocomposites for adsorption and catalytic oxidation in water treatment applications. Open Chem 18:1148–1166. https://doi.org/10.1515/chem-2020-0159
22. Tahir MB, Iqbal T, Kiran H, Hasan A (2019) Insighting role of reduced graphene oxide in BiVO4 nanoparticles for improved photocatalytic hydrogen evolution and dyes degradation. Int J Energy Res 43:2410–2417. https://doi.org/10.1002/er.4443
23. Rafique M, Sadaf I, Tahir MB, Rafique MS, Nabi G, Iqbal T, Sughra K (2019) Novel and facile synthesis of silver nanoparticles using Albizia procera leaf extract for dye degradation and antibacterial applications. Mater Sci Eng C 99:1313–1324. https://doi.org/10.1016/j.msec.2019.02.059

24. Castro-Muñoz R (2020) The role of new inorganic materials in composite membranes for water disinfection. Membranes (Basel). https://doi.org/10.3390/membranes10050101
25. Rafique M, Nawaz H, Shahid Rafique M, Bilal Tahir M, Nabi G, Khalid NR (2019) Material and method selection for efficient solid oxide fuel cell anode: Recent advancements and reviews. Int J Energy Res 43:2423–2446. https://doi.org/10.1002/er.4210
26. Abboud M, Youssef S, Podlecki J, Habchi R, Germanos G, Foucaran A (2015) Superparamagnetic Fe3O4 nanoparticles, synthesis and surface modification. Mater Sci Semicond Process 39:641–648. https://doi.org/10.1016/J.MSSP.2015.05.035
27. Gong P, Yu J, Sun H, Hong J, Zhao S, Xu D, Yao S (2006) Preparation and characterization of OH-functionalized magnetic nanogels under UV irradiation. J Appl Polym Sci 101:1283–1290. https://doi.org/10.1002/app.23250
28. Afsheen S, Tahir MB, Iqbal T, Liaqat A, Abrar M (2018) Green synthesis and characterization of novel iron particles by using different extracts. J Alloys Compd 732:935–944. https://doi.org/10.1016/j.jallcom.2017.10.137
29. Yadav GD, Bokade VV (1996) Novelties of heteropoly acid supported on clay: etherification of phenethyl alcohol with alkanols. Appl Catal A Gen 147:299–323. https://doi.org/10.1016/S0926-860X(96)00206-2
30. K. Y Nandiwale, P. S Niphadkar, V. V Bokade, Synthesis of Oxygenated Fuel Additives via Acetylation of Bio-Glycerol over H2SO4 Modified Montmorillonite K10 Catalyst, Prog. Petrochemical Sci. 1 (2018). https://doi.org/10.31031/PPS.2018.01.000501.
31. Bhandari S, Kasana V (2018) Fe3+-montmorillonite K10 as an efficient, green and reusable heterogeneous catalyst for synthesis of mannich type reaction under solvent-free condition. Int Res J Pure Appl Chem 16:1–11. https://doi.org/10.9734/IRJPAC/2018/41983
32. Marsh A, Heath A, Patureau P, Evernden M, Walker P (2018) Alkali activation behaviour of un-calcined montmorillonite and illite clay minerals. Appl Clay Sci 166:250–261. https://doi.org/10.1016/J.CLAY.2018.09.011
33. Sadegh H, Shahryari-ghoshekandi R, Kazemi M (2014) Study in synthesis and characterization of carbon nanotubes decorated by magnetic iron oxide nanoparticles. Int Nano Lett 4:129–135. https://doi.org/10.1007/s40089-014-0128-1
34. Mascolo M, Pei Y, Ring T, Mascolo MC, Pei Y, Ring TA (2013) Room temperature Co-precipitation synthesis of magnetite nanoparticles in a large ph window with different bases. Mater. (Basel) 6:5549–5567. https://doi.org/10.3390/ma6125549
35. Tahir MB, Rafique M, Isa Khan M, Majid A, Nazar F, Sagir M, Gilani S, Farooq M, Ahmed A (2018) Enhanced photocatalytic hydrogen energy production of g-C3N4-WO3 composites under visible light irradiation. Int J Energy Res 42:4667–4673. https://doi.org/10.1002/er.4208
36. Lu H, Wang J, Li F, Huang X, Tian B, Hao H (2018) Highly efficient and reusable montmorillonite/Fe3O4/humic acid nanocomposites for simultaneous removal of Cr(VI) and aniline. Nanomaterials 8:537. https://doi.org/10.3390/nano8070537
37. Lu W, Shen Y, Xie A, Zhang W (2010) Green synthesis and characterization of superparamagnetic Fe3O4 nanoparticles. J Magn Magn Mater 322:1828–1833. https://doi.org/10.1016/J.JMMM.2009.12.035
38. Jubb AM, Allen HC (2010) Vibrational spectroscopic characterization of hematite, maghemite, and magnetite thin films produced by vapor deposition. ACS Appl Mater Interfaces 2:2804–2812. https://doi.org/10.1021/am1004943
39. Rani S, Varma GD (2015) Superparamagnetism and metamagnetic transition in Fe3O4 nanoparticles synthesized via co-precipitation method at different pH. Phys B Condens Matter 472:66–77. https://doi.org/10.1016/j.physb.2015.05.016
40. Gu Z, Gao M, Luo Z, Lu L, Ye Y, Liu Y (2014) Bis-pyridinium dibromides modified organo-bentonite for the removal of aniline from wastewater: a positive role of π–π polar interaction. Appl Surf Sci 290:107–115. https://doi.org/10.1016/J.APSUSC.2013.11.008
41. Kozak M, Domka L (2004) Adsorption of the quaternary ammonium salts on montmorillonite. J Phys Chem Solids 65:441–445. https://doi.org/10.1016/J.JPCS.2003.09.015
42. Thommes M, Kaneko K, Neimark AV, Olivier JP, Rodriguez-Reinoso F, Rouquerol J, Sing KSW (2015) Physisorption of gases, with special reference to the evaluation of surface area and pore size distribution (IUPAC technical report). Pure Appl Chem 87:1051–1069. https://doi.org/10.1515/pac-2014-1117
43. Ursino C, Castro-Muñoz R, Drioli E, Gzara L, Albeirutty MH, Figoli A (2018) Progress of nanocomposite membranes for water treatment. Membranes (Basel). https://doi.org/10.3390/membranes8020018
44. Castro-Muñoz R, Gontarek E, Figoli A (2019) Membranes for toxic- and heavy-metal removal. In: Current Trends and Future Developments on (Bio-) Membranes. Elsevier Inc., pp 125–149. https://doi.org/10.1016/B978-0-12-816778-6.00007-2
45. Zare K, Sadegh H, Shahryari-ghoshekandi R, Asif M, Tyagi I, Agarwal S, Gupta VK (2016) Equilibrium and kinetic study of ammonium ion adsorption by Fe3O4 nanoparticles from aqueous solutions. J Mol Liq 213:345–350. https://doi.org/10.1016/J.MOLLIQ.2015.08.045
46. Copcia V, Hristodor C, Luchian C, Bilba N, Sandu I (2010) Ammonium nitrogen removal from aqueous solution by natural clay. Rev Chim (Bucharest) 61:1192–1196
47. Liu H, Peng S, Shu L, Chen T, Bao T, Frost RL (2013) Effect of Fe3O4 addition on removal of ammonium by zeolite NaA. J Colloid Interface Sci 390:204–210. https://doi.org/10.1016/J.JCIS.2012.09.010
48. Cowan CT, White D (1958) The mechanism of exchange reactions occurring between sodium montmorillonite and various n-primary aliphatic amine salts. Trans Faraday Soc 54:691–697. https://doi.org/10.1039/TF9585400691
49. Rožić M, Cerjan-Stefanović Š, Kurajica S, Vančina V, Hodžić E (2000) Ammoniacal nitrogen removal from water by treatment with clays and zeolites. Water Res 34:3675–3681. https://doi.org/10.1016/S0043-1354(00)00113-5
50. Wang J, Zheng S, Shao Y, Liu J, Xu Z, Zhu D (2010) Amino-functionalized Fe3O4@SiO2 core–shell magnetic nanomaterial as a novel adsorbent for aqueous heavy metals removal. J Colloid Interface Sci 349:293–299. https://doi.org/10.1016/J.JCIS.2010.05.010
51. Cheng Y, Huang T, Shi X, Wen G, Sun Y (2017) Removal of ammonium ion from water by Na-rich birnessite: performance and mechanisms. J Environ Sci 57:402–410. https://doi.org/10.1016/J.JES.2016.11.015
52. Langmuir I (1918) The adsorption of gases on plane surfaces of glass, mica and platinum. J Am Chem Soc 40:1361–1403. https://doi.org/10.1021/ja02242a004
53. Freundlich HMF (1906) Over the adsorption in solution. J Phys Chem 57:1100–1107
54. Saadi R, Saadi Z, Fazaeli R, Fard NE (2015) Monolayer and multilayer adsorption isotherm models for sorption from aqueous media. Korean J Chem Eng 32:787–799. https://doi.org/10.1007/s11814-015-0053-7
55. Sips R (1948) Combined form of Langmuir and Freundlich equations. J Chem Phys 16:490–495
56. Srivastava V, Sharma YC, Sillanpää M (2015) Application of nano-magnesso ferrite (n-MgFe2O4) for the removal of Co2+ ions from synthetic wastewater: kinetic, equilibrium and thermodynamic studies. Appl Surf Sci 338:42–54. https://doi.org/10.1016/J.APSUSC.2015.02.072

57. Srivastava V, Weng CH, Singh VK, Sharma YC (2011) Adsorption of nickel ions from aqueous solutions by nano alumina: kinetic, mass transfer, and equilibrium studies. J Chem Eng Data 56:1414–1422. https://doi.org/10.1021/je101152b
58. Chen L, Chen XL, Zhou CH, Yang HM, Ji SF, Tong DS, Zhong ZK, Yu WH, Chu MQ (2017) Environmental-friendly montmorillonite-biochar composites: Facile production and tunable adsorption-release of ammonium and phosphate. J Clean Prod 156:648–659. https://doi.org/10.1016/J.JCLEPRO.2017.04.050
59. Mazloomi F, Jalali M (2017) Adsorption of ammonium from simulated wastewater by montmorillonite nanoclay and natural vermiculite: experimental study and simulation. Environ Monit Assess 189:415. https://doi.org/10.1007/s10661-017-6080-6
60. Qiu H, Lv L, Pan B, Zhang Q, Zhang W, Zhang Q (2009) Critical review in adsorption kinetic models. J Zhejiang Univ A 10:716–724. https://doi.org/10.1631/jzus.A0820524
61. Iftekhar S, Srivastava V, Casas A, Sillanpää M (2018) Synthesis of novel GA-g-PAM/SiO2 nanocomposite for the recovery of rare earth elements (REE) ions from aqueous solution. J Clean Prod 170:251–259. https://doi.org/10.1016/J.JCLEPRO.2017.09.166
62. Castro-Muñoz R, González-Melgoza LL, García-Depraect O (2021) Ongoing progress on novel nanocomposite membranes for the separation of heavy metals from contaminated water. Chemosphere 270:129421. https://doi.org/10.1016/j.chemosphere.2020.129421
63. Castro-Muñoz R (2020) The strategy of nanomaterials in polymeric membranes for water treatment: nanocomposite membranes. Tecnol y Ciencias Del Agua. 11: 410–436. https://doi.org/10.24850/j-tyca-2020-01-11

Authors and Affiliations

Jianzhi Song[1] · Varsha Srivastava[1] · Tomas Kohout[2] · Mika Sillanpää[3,4,5,6,7,8] · Tuomo Sainio[1]

1 Department of Separation Science, School of Engineering Science, LUT University, Sammonkatu 12, 50130 Mikkeli, Finland

2 Department of Geosciences and Geography, University of Helsinki, Helsinki, Finland

3 Department of Chemical Engineering, School of Mining, Metallurgy and Chemical Engineering, University of Johannesburg, P. O. Box 17011, Doornfontein 2028, South Africa

4 School of Chemical and Metallurgical Engineering, University of the Witwatersrand, Johannesburg 2050, South Africa

5 Chemistry Department, College of Science, King Saud University, Riyadh 11451, Saudi Arabia

6 Department of Biological and Chemical Engineering, Aarhus University, Nørrebrogade 44, 8000 Aarhus C, Denmark

7 Faculty of Science and Technology, School of Applied Physics, University Kebangsaan Malaysia, 43600 Bangi, Selangor, Malaysia

8 International Research Centre of Nanotechnology for Himalayan Sustainability (IRCNHS), Shoolini University, Solan 173212, Himachal Pradesh, India